A model for filtered backprojection reconstruction artifacts due to time-varying attenuation values in perfusion C-arm CT

Andreas Fieselmann[1,2,3], Frank Dennerlein[3],
Yu Deuerling-Zheng[3], Jan Boese[3], Rebecca Fahrig[4] and
Joachim Hornegger[1,2]

[1]Department of Computer Science, Pattern Recognition Lab,
Friedrich-Alexander University of Erlangen-Nuremberg, Martensstr. 3, 91058 Erlangen, Germany
[2]Erlangen Graduate School in Advanced Optical Technologies (SAOT),
Erlangen, Germany
[3]Siemens AG, Healthcare Sector, Angiography & Interventional X-Ray Systems,
Siemensstr. 1, 91301 Forchheim, Germany
[4]Department of Radiology, Lucas MRS Center, Stanford University, 1201 Welch Road, Palo Alto, CA 94305, USA

E-mail: `andreas.fieselmann@informatik.uni-erlangen.de`

Abstract. Filtered backprojection is the basis for many CT reconstruction tasks. It assumes constant attenuation values of the object during the acquisition of the projection data. Reconstruction artifacts can arise if this assumption is violated. For example, contrast flow in perfusion imaging with C-arm CT systems, which have acquisition times of several seconds per C-arm rotation, can cause this violation. In this paper, we derived and validated a novel spatio-temporal model to describe these kinds of artifacts. The model separates the temporal dynamics due to contrast flow from the scan and reconstruction parameters. We introduced derivative-weighted point spread functions to describe the spatial spread of the artifacts. The model allows prediction of reconstruction artifacts for given temporal dynamics of the attenuation values. Furthermore, it can be used to systematically investigate the influence of different reconstruction parameters on the artifacts. We have shown that with optimized redundancy weighting function parameters the spatial spread of the artifacts around a typical arterial vessel can be reduced by about 70%. Finally, an inversion of our model could be used as the basis for novel dynamic reconstruction algorithms that further minimize these artifacts.

PACS numbers: 87.59.bd, 87.57.N-, 47.63.Jd, 87.57.C-, 87.19.U-

(a) C-arm CT system.

(b) Acquisition geometry.
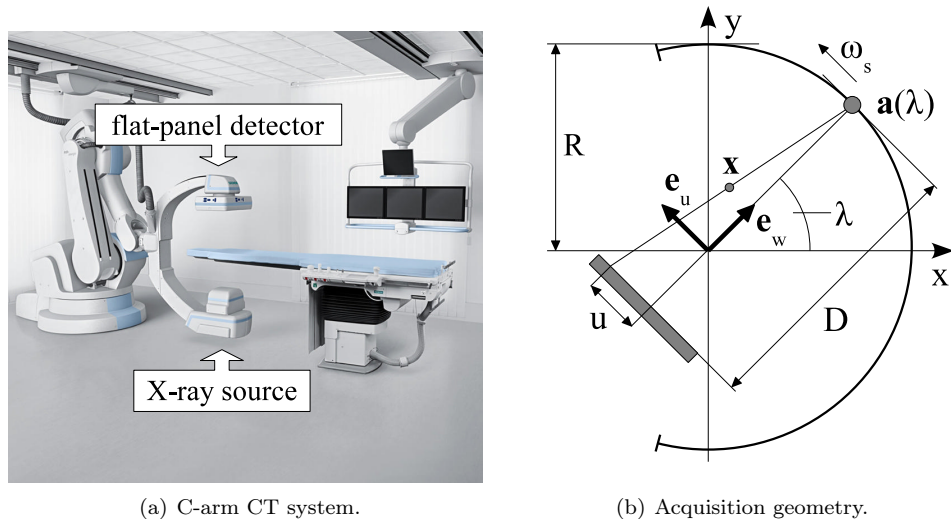
Figure 1. (a) C-arm angiography system capable of CT-like imaging (Artis zeego, Siemens AG, Healthcare Sector, Forchheim, Germany) and (b) illustration of the acquisition geometry described in Section 2.

1. Introduction

1.1. Clinical background

Perfusion CT and MR imaging are used for stroke diagnosis. In perfusion CT an iodinated contrast bolus is injected and the contrast is then tracked in reconstructed images that are obtained at typically one image per second over 40–50 seconds. Perfusion parameters such as cerebral blood flow and volume, mean transit time and time-to-peak are computed by analyzing the local time-attenuation curves in each of the reconstructed voxels (Shetty & Lev 2006). Following diagnosis, a catheter-guided stroke therapy procedure, supported by 2-D images from a C-arm angiography system (Figure 1(a)), can be performed in selected patients.

Nowadays, C-arm systems are also capable of CT-like imaging (C-arm CT). During a typical rotation of the C-arm through 200°, projections are acquired and standard algorithms are used to reconstruct a 3-D volume data set (Strobel et al. 2009). Similar to conventional perfusion CT, a C-arm CT system could be used for perfusion imaging by generating a sequence of reconstructed CT volumes from multiple C-arm rotations. The intra-procedural perfusion information could, for example, help to determine the treatment progress and endpoint during a stroke intervention.

Wintermark et al. (2004) have shown that a sample period of one volume every 3 seconds, each acquired in about 0.5 seconds, can provide sufficient information for perfusion measurement. However, in C-arm CT imaging both the sample period and the acquisition time are typically 3–5 seconds due to the slow rotation of a C-arm system. This leads to an inconsistent set of projections caused by the (intentional) change of contrast concentration during the acquisition time and can result in reconstruction artifacts. To date there have been very few approaches to handle these inconsistencies. Neukirchen et al. (2010) have proposed an iterative

reconstruction technique which, however, leads to a high computational complexity and long reconstruction times. Since time is a critical factor in stroke therapy fast reconstruction algorithms for the large-volume data sets are needed. Fieselmann et al. (2010) have presented a reconstruction approach based on the filtered backprojection (FBP) that can be computationally very fast if implemented using modern graphics hardware (Rohkohl et al. 2009).

For the analysis and optimization of FBP-based reconstruction algorithms a good understanding of artifacts due to time-varying attenuation values is essential. In this paper, we present a novel spatio-temporal model for these kinds of artifacts. This model can be applied to estimate the magnitude of artifacts and to optimize reconstruction parameters. It can also be used to develop new FBP-based dynamic reconstruction algorithms.

1.2. Previous work

There exists some previous work that concerns FBP reconstruction artifacts due to time-varying attenuation values. Holden & Ip (1978) presented a mathematical formalism to describe these artifacts in parallel-beam geometry CT scanning and validated it using computer simulations. But their formalism assumes periodic changes of contrast concentration and is therefore not suitable to describe artifacts in perfusion imaging with time-attenuation curves that are non-periodic. The work of Ip et al. (1983) and Garden et al. (1984) also show reconstructions using computer simulation of objects with time-varying attenuations during the scanning but no mathematical analyses of the artifacts were carried out. Similar reconstruction problems as mentioned above arise in dynamic SPECT when the tracer concentration changes during one camera rotation. Bok et al. (1987) and Nakajima et al. (1992) used FBP reconstruction for dynamic SPECT and investigated the resulting artifacts qualitatively and quantitatively but without derivation of a model. By using a C-arm mounted X-ray image intensifier for 3-D imaging Fahrig (1999) investigated FBP reconstruction artifacts due to the time-varying opacification of a vessel but no mathematical model was developed. Recently, Montes & Lauritsch (2007) studied artifacts due to time-varying contrast concentration in perfusion CT with a slowly rotating CT scanner. Their formalism models the reconstruction error of a time-attenuation curve as a low-pass filtering process. However, they did not study how artifacts propagate into other reconstructed voxel attenuation values in the image, which is the focus of this work.

2. Background of FBP reconstruction

In this section we will present our notation with a brief description of the direct 2-D fan-beam FBP reconstruction. A more detailed description of these methods can be found in Kak & Slaney (1988).

The X-ray source rotates with a constant angular velocity ω_s on a circular path of radius R around the origin of the coordinate system (Figure 1(b)). The location $\boldsymbol{a}(\lambda(t))$ of the source at time t is given by

$$\boldsymbol{a}(\lambda(t)) = (R\cos(\lambda(t)),\, R\sin(\lambda(t)))^{\mathrm{T}} \tag{1}$$

$$\lambda(t) = \omega_s\, t + \lambda_0 \tag{2}$$

where $\lambda(t)$ is the view-angle and λ_0 is the starting view-angle at $t = 0$. In this paper, the variable λ always depends explicitly on t although this is not always indicated for simplicity. We define the unit vectors:

$$\boldsymbol{e}_{\mathrm{u}}(\lambda) = (-\sin(\lambda),\, \cos(\lambda))^{\mathrm{T}} \tag{3}$$

$$\boldsymbol{e}_{\mathrm{w}}(\lambda) = (\cos(\lambda),\, \sin(\lambda))^{\mathrm{T}} \ . \tag{4}$$

The function $u^*(\boldsymbol{x}, \lambda)$ gives the coordinate where a ray from source location $\boldsymbol{a}(\lambda)$ passing through $\boldsymbol{x}$ intersects the detector. It can be computed as

$$u^*(\boldsymbol{x}, \lambda) = \frac{D\,\boldsymbol{x} \cdot \boldsymbol{e}_{\mathrm{u}}(\lambda)}{R - \boldsymbol{x} \cdot \boldsymbol{e}_{\mathrm{w}}(\lambda)} \tag{5}$$

where the dot denotes a scalar product and D is the source-to-detector distance. We assume that the attenuation values $\mu(\boldsymbol{x}, \lambda)$ at locations $\boldsymbol{x} = (x, y)^{\mathrm{T}}$ have view-angle-dependent values. We further assume that no truncation of the projection images occurs and that the attenuation values are zero in the region $x^2 + y^2 \geq R^2$.

The projection $p(\lambda, u)$, which is measured at the detector coordinate u, can be written using the usual definition of the delta function:

$$p(\lambda, u) = \iint \mu(\boldsymbol{x}, \lambda)\, \delta(u^*(\boldsymbol{x}, \lambda) - u)\, \mathrm{d}x\, \mathrm{d}y \ . \tag{6}$$

In this paper, all integrals without explicit integration endpoints should be interpreted as the limit value when the lower and upper endpoints approach $-\infty$ and $+\infty$, respectively. We can reconstruct the pixel value $\mu_{\mathrm{rec}}(\boldsymbol{r}, t_{\mathrm{rec}})$ at location $\boldsymbol{r}$ corresponding to the state at time t_{rec} using the FBP reconstruction with an angular sliding window function $w_\Lambda(\lambda, \gamma)$:

$$\mu_{\mathrm{rec}}(\boldsymbol{r}, t_{\mathrm{rec}}) = \int \frac{R\,D}{(R - \boldsymbol{r} \cdot \boldsymbol{e}_{\mathrm{w}}(\lambda(t)))^2}\, \int p(\lambda(t), u)\, h_{\mathrm{ramp}}\Big(u^*(\boldsymbol{r}, \lambda(t)) - u\Big)$$

$$\times\, \frac{D}{(u^2 + D^2)^{1/2}}\, w_\Lambda\Big(\lambda(t) - \lambda(t_{\mathrm{rec}}),\, \arctan(u/D)\Big)\, \mathrm{d}u\, \mathrm{d}t \ . \tag{7}$$

Here $h_{\mathrm{ramp}}(u)$ denotes the usual ramp filter kernel and $\gamma = \arctan(u/D)$ is the fan-angle. This reconstruction formula assumes a consistent data set of projection images, i.e. there is no change of the attenuation values over time. The function $w_\Lambda(\lambda, \gamma)$ is zero outside an angular interval of size Λ:

$$w_\Lambda(\lambda, \gamma) = \begin{cases} m_\Lambda(\lambda + \Lambda/2, \gamma) & \text{if } -\Lambda/2 \leq \lambda \leq \Lambda/2 \\ 0 & \text{otherwise} \ . \end{cases} \tag{8}$$

The minimum interval for Λ is the short-scan range $\pi + \gamma_{\mathrm{m}}$ where γ_{m} is the full fan-angle. The function $m_\Lambda(\lambda, \gamma)$ compensates for redundant data inside the angular interval due to the fan-beam acquisition geometry. An example for $m_\Lambda(\lambda, \gamma)$ is the weighting function proposed by Silver (2000),

$$m_\Lambda(\lambda, \gamma) = \begin{cases} \sin^2\left(\dfrac{\pi}{4}\,\dfrac{\lambda}{\Gamma/2 + \gamma}\right) & \text{if } 0 \leq \lambda < \Gamma + 2\gamma \\[2ex] 1 & \text{if } \Gamma + 2\gamma \leq \lambda < \pi + 2\gamma \\[2ex] \sin^2\left(\dfrac{\pi}{4}\,\dfrac{\pi + \Gamma - \lambda}{\Gamma/2 - \gamma}\right) & \text{if } \pi + 2\gamma \leq \lambda < \pi + \Gamma \\[2ex] 0 & \text{otherwise} \ , \end{cases} \tag{9}$$

with $\Gamma = \Lambda - \pi$. With the definition of the FBP from Equation (7) that uses the window $w_\Lambda(\lambda, \gamma)$ we can reconstruct an image corresponding to a certain time point t_{rec}. The time point could be flexibly chosen if the C-arm system could perform continuous C-arm rotations. With current C-arm systems the C-arm rotates in alternating directions therefore the choice for t_{rec} is restricted to the time point at the center during one short-scan rotation. The artifact model in Section 3 is applicable to both scenarios, continuous and bi-directional C-arm rotations.

3. Spatio-temporal artifact model

In this section we will derive and interpret our novel artifact model. The key idea of this model is to separate the artifact into two components, one that depends on the dynamic process, i.e. the change of attenuation values, and one that depends on the acquisition geometry and the reconstruction algorithm parameters.

3.1. Derivation

We substitute the expression from Equation (6) into Equation (7) and change the order of integration such that we obtain:

$$
\mu_{\mathrm{rec}}(\boldsymbol{r}, t_{\mathrm{rec}}) = \iiiint \frac{R\,D^2}{(R - \boldsymbol{r} \cdot \boldsymbol{e}_{\mathrm{w}}(\lambda(t)))^2}\, \mu(\boldsymbol{x}, \lambda(t))\, h_{\mathrm{ramp}}\Big(u^*(\boldsymbol{r}, \lambda(t)) - u\Big)
$$
$$
\times \Big(u^2 + D^2\Big)^{-1/2} w_\Lambda\Big(\lambda(t) - \lambda(t_{\mathrm{rec}}), \arctan(u/D)\Big)
$$
$$
\times \delta(u^*(\boldsymbol{x}, \lambda(t)) - u)\,\mathrm{d}u\,\mathrm{d}t\,\mathrm{d}x\,\mathrm{d}y\,. \tag{10}
$$

We evaluate the delta function and re-arrange the result into the following two functions (see Appendix A for details):

$$
\mu_{\mathrm{rec}}(\boldsymbol{r}, t_{\mathrm{rec}}) = \iint \chi(\boldsymbol{r} - \boldsymbol{x}, \boldsymbol{x}, t_{\mathrm{rec}})\,\mathrm{d}x\,\mathrm{d}y \tag{11}
$$

$$
\chi(\boldsymbol{s}, \boldsymbol{x}, t_{\mathrm{rec}}) = \int \frac{R\,D^2}{(R - (\boldsymbol{s} + \boldsymbol{x}) \cdot \boldsymbol{e}_{\mathrm{w}}(\lambda(t)))^2}\, h_{\mathrm{ramp}}\Big(u^*(\boldsymbol{s} + \boldsymbol{x}, \lambda(t)) - u^*(\boldsymbol{x}, \lambda(t))\Big)
$$
$$
\times \mu\Big(\boldsymbol{x}, \lambda(t)\Big) \Big((u^*(\boldsymbol{x}, \lambda(t)))^2 + D^2\Big)^{-1/2}
$$
$$
\times w_\Lambda\Big(\lambda(t) - \lambda(t_{\mathrm{rec}}), \arctan(u^*(\boldsymbol{x}, \lambda(t))/D)\Big)\,\mathrm{d}t\,. \tag{12}
$$

The function $\chi(\boldsymbol{s}, \boldsymbol{x}, t_{\mathrm{rec}})$ can be interpreted as the reconstruction associated with a point object located at $\boldsymbol{x}$ which has time-varying attenuation values $\mu(\boldsymbol{x}, \lambda(t))$. The variable $\boldsymbol{s} = (s_x, s_y)^{\mathrm{T}}$ denotes the distance vector from the point object in the reconstructed image and t_{rec} is the temporal center of the sliding window used in the FBP reconstruction. A detailed interpretation of $\chi(\boldsymbol{s}, \boldsymbol{x}, t_{\mathrm{rec}})$ will be given in Section 3.2.

We now focus on the time dependence of $\mu(\boldsymbol{x}, \lambda(t))$. We start by assuming that it is a smooth function without discontinuities. This assumption is reasonable when an intra-venous contrast bolus injection, which is the standard injection method in brain perfusion CT and MR imaging, is used. If injected into the antecubital vein, for example, the bolus will pass through the heart and lungs. Thus, when it arrives in

the brain it has been low-pass filtered and is a smooth curve. Using this assumption we can represent $\mu(\boldsymbol{x}, \lambda(t))$ as a Taylor series around $\lambda(t_{\text{rec}})$:

$$\mu(\boldsymbol{x}, \lambda(t)) = \sum_{n=0}^{\infty} \frac{\mathrm{d}^n \mu(\boldsymbol{x}, \lambda(t))}{\mathrm{d}\lambda^n} \bigg|_{\lambda(t)=\lambda(t_{\text{rec}})} \frac{(\lambda(t) - \lambda(t_{\text{rec}}))^n}{n!} \ . \tag{13}$$

According to Equation (2) the second-order derivative of $\lambda(t)$ is zero. Therefore, we have the following total derivative (the proof is given in Appendix B):

$$\begin{aligned}
\frac{\mathrm{d}^n \mu(\boldsymbol{x}, \lambda(t))}{\mathrm{d}t^n} \bigg|_{t=t_{\text{rec}}} &= \frac{\partial^n \mu(\boldsymbol{x}, \lambda(t))}{\partial \lambda^n} \bigg|_{\lambda(t)=\lambda(t_{\text{rec}})} \left(\frac{\mathrm{d}\lambda(t)}{\mathrm{d}t} \bigg|_{t=t_{\text{rec}}} \right)^n \\
&= \frac{\mathrm{d}^n \mu(\boldsymbol{x}, \lambda(t))}{\mathrm{d}\lambda^n} \bigg|_{\lambda(t)=\lambda(t_{\text{rec}})} \omega_{\text{s}}^n \ .
\end{aligned} \tag{14}$$

We combine Equation (14) and Equation (13) and plug the new expression for $\mu(\boldsymbol{x}, \lambda(t))$ into Equation (12). Then we change the order of summation and integration and split the result into these two functions

$$\chi(\boldsymbol{s}, \boldsymbol{x}, t_{\text{rec}}) = \sum_{n=0}^{\infty} \frac{\mathrm{d}^n \mu(\boldsymbol{x}, t)}{\mathrm{d}t^n} \bigg|_{t=t_{\text{rec}}} \omega_{\text{s}}^{-n} \, P_n(\boldsymbol{s}, \boldsymbol{x}, \lambda(t_{\text{rec}})) \tag{15}$$

$$\begin{aligned}
P_n(\boldsymbol{s}, \boldsymbol{x}, \lambda_{\text{rec}}) = R\, D^2 \int &\frac{(\lambda - \lambda_{\text{rec}})^n}{n!} \left(R - (\boldsymbol{s} + \boldsymbol{x}) \cdot \boldsymbol{e}_{\text{w}}(\lambda) \right)^{-2} \\
&\times h_{\text{ramp}} \Big(u^*(\boldsymbol{s} + \boldsymbol{x}, \lambda) - u^*(\boldsymbol{x}, \lambda) \Big) \\
&\times \Big((u^*(\boldsymbol{x}, \lambda))^2 + D^2 \Big)^{-1/2} \\
&\times w_{\Lambda} \Big(\lambda - \lambda_{\text{rec}}, \arctan((u^*(\boldsymbol{x}, \lambda))/D) \Big) \, \mathrm{d}\lambda
\end{aligned} \tag{16}$$

where we defined $\lambda_{\text{rec}} \equiv \lambda(t_{\text{rec}})$. We substitute λ by $\lambda + \lambda_{\text{rec}}$ and use Equation (8) to determine the integration interval such that we get:

$$\begin{aligned}
P_n(\boldsymbol{s}, \boldsymbol{x}, \lambda_{\text{rec}}) = R\, D^2 \int_{-\Lambda/2}^{+\Lambda/2} &\frac{\lambda^n}{n!} \left(R - (\boldsymbol{s} + \boldsymbol{x}) \cdot \boldsymbol{e}_{\text{w}}(\lambda + \lambda_{\text{rec}}) \right)^{-2} \\
&\times h_{\text{ramp}} \Big(u^*(\boldsymbol{s} + \boldsymbol{x}, \lambda + \lambda_{\text{rec}}) - u^*(\boldsymbol{x}, \lambda + \lambda_{\text{rec}}) \Big) \\
&\times \Big((u^*(\boldsymbol{x}, \lambda + \lambda_{\text{rec}}))^2 + D^2 \Big)^{-1/2} \\
&\times w_{\Lambda} \Big(\lambda, \arctan((u^*(\boldsymbol{x}, \lambda + \lambda_{\text{rec}}))/D) \Big) \, \mathrm{d}\lambda \ .
\end{aligned} \tag{17}$$

Equations (11), (15) and (17) constitute our artifact model that we will interpret in the following section.

3.2. Interpretation

According to Equation (11) the reconstructed image $\mu_{\text{rec}}(\boldsymbol{r}, t_{\text{rec}})$ is the superposition of the functions $\chi(\boldsymbol{s}, \boldsymbol{x}, t_{\text{rec}})$. In a theoretically exact reconstruction with $\mu_{\text{rec}}(\boldsymbol{r}, t_{\text{rec}}) = \mu(\boldsymbol{r}, t_{\text{rec}})$ this function would be:

$$\chi_{\text{theoretical}}(\boldsymbol{s}, \boldsymbol{x}, t_{\text{rec}}) = \delta(\boldsymbol{s})\, \mu(\boldsymbol{x}, t_{\text{rec}}) \ . \tag{18}$$

However, in reality due to the finite detector pixel width not all spatial frequencies in the projections can be measured and the ramp filter kernel has to be adapted.
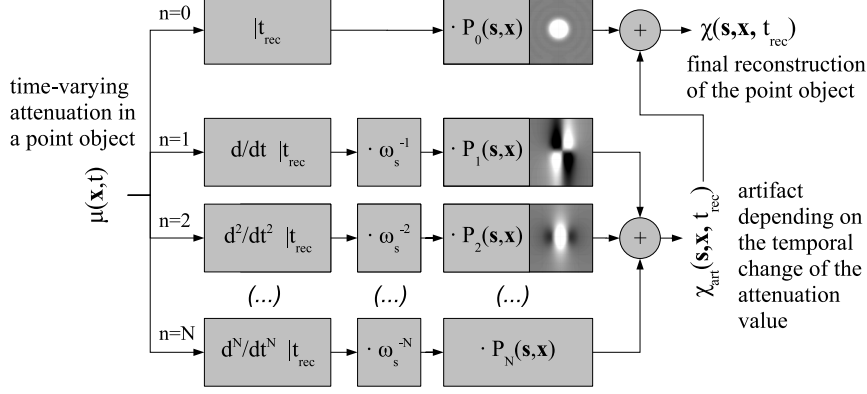
Figure 2. Spatio-temporal artifact model: a point object at $\boldsymbol{x}$ with time-varying attenuation value $\mu(\boldsymbol{x}, t)$ creates an artifact around $\boldsymbol{x}$ in the reconstructed image. The artifact is described by $\chi_{\text{art}}(\boldsymbol{s}, \boldsymbol{x}, t_{\text{rec}})$ where $\boldsymbol{s}$ is the distance vector from $\boldsymbol{x}$. This function is the sum of the functions $P_n(\boldsymbol{s}, \boldsymbol{x})$ that are each weighted with the n-th derivative of $\mu(\boldsymbol{x}, t)$, which is evaluated at the central time point t_{rec} of the set of projection data, and a C-arm-angular-velocity-(ω_{s})-dependent factor. The final reconstruction $\chi(\boldsymbol{s}, \boldsymbol{x}, t_{\text{rec}})$ is a superposition of the artifact χ_{art} and the product $\mu(\boldsymbol{x}, t_{\text{rec}})P_0(\boldsymbol{s}, \boldsymbol{x})$ where P_0 denotes the (conventional) point spread function due to the scanning and reconstruction process.

The reconstruction of a point object will then lead to a slightly blurred point object with a smooth edge. The point spread function (PSF) provides a description of the blurring (Ohkubo et al. 2009). We denote by $P_{\text{static}}(\boldsymbol{s}, \boldsymbol{x})$ the PSF that characterizes the scanning and reconstruction process of a static, time-independent point object at $\boldsymbol{x}$ and get:

$$\chi_{\text{static}}(\boldsymbol{s}, \boldsymbol{x}, t_{\text{rec}}) = P_{\text{static}}(\boldsymbol{s}, \boldsymbol{x}) \, \mu(\boldsymbol{x}, t_{\text{rec}}) \,. \tag{19}$$

We can interpret Equation (19) and Equation (11) as transformations of the true attenuation values μ into the reconstructed attenuation values μ_{rec}. The function $P_{\text{static}}(\boldsymbol{s}, \boldsymbol{x})$ is shift-variant because it depends explicitly on $\boldsymbol{x}$. In the fan-beam FBP this property is evidenced by a non-uniform noise propagation (Zeng 2004), for example.

In Equation (15) the variable $\lambda(t_{\text{rec}})$ is a system parameter that is determined by the start and end scan angle. For a time-independent object, i.e. when $\mathrm{d}\mu(\boldsymbol{x}, t)/\mathrm{d}t = 0$, Equation (15) reduces to Equation (19). However, Equation (15) is more general because it has been derived for dynamic, time-dependent objects. In this equation, the function $\chi(\boldsymbol{s}, \boldsymbol{x}, t_{\text{rec}})$ is a superposition of weighted functions which we denote by $P_n(\boldsymbol{s}, \boldsymbol{x})$. The weights are the n-th order derivative values of $\mu(\boldsymbol{x}, t)$, evaluated at t_{rec}, and the n-th power of $1/\omega_{\text{s}}$. Because the functions P_n with $n \geq 1$ have a similar character as P_0 we denote them as n-th order derivative-weighted point spread functions (DWPSF).

We can split $\chi(\boldsymbol{s}, \boldsymbol{x}, t_{\text{rec}})$ into a term corresponding to the static case as in Equation (19) and into terms that depend on first or higher order derivatives of $\mu(\boldsymbol{x}, t)$:

$$\chi(\boldsymbol{s}, \boldsymbol{x}, t_{\text{rec}}) = \mu(\boldsymbol{x}, t_{\text{rec}}) \, P_0(\boldsymbol{s}, \boldsymbol{x}, \lambda(t_{\text{rec}})) + \chi_{\text{art}}(\boldsymbol{s}, \boldsymbol{x}, t_{\text{rec}}) \tag{20}$$

$$\chi_{\text{art}}(\boldsymbol{s}, \boldsymbol{x}, t_{\text{rec}}) = \sum_{n=1}^{\infty} \left. \frac{\mathrm{d}^n \mu(\boldsymbol{x}, t)}{\mathrm{d}t^n} \right|_{t=t_{\text{rec}}} \omega_{\text{s}}^{-n} \, P_n(\boldsymbol{s}, \boldsymbol{x}, \lambda(t_{\text{rec}})) \,. \tag{21}$$

We call $\chi_{\mathrm{art}}(\boldsymbol{s}, \boldsymbol{x}, t_{\mathrm{rec}})$ the artifact function that results from a time-varying attenuation value $\mu(\boldsymbol{x}, \lambda(t))$ at $\boldsymbol{x}$. The artifact is centered around $\boldsymbol{x}$ and the vector $\boldsymbol{s}$ gives the distance from the center. Figure 2 shows an illustration of the artifact model where for simplicity the scan geometry variable λ_{rec} has been omitted. Furthermore, in this illustration the infinite sum is approximated by the finite sum from $n = 1$ to $n = N$.

Each term in the artifact model consists of two components. The first component is the rate-of-change of the time-attenuation curve — given by its temporal derivative value — relative to the C-arm rotation speed. The second component is the function $P_n(\boldsymbol{s}, \boldsymbol{x}, \lambda_{\mathrm{rec}})$ that depends only on the scan geometry $(R, D, \Lambda, \lambda_{\mathrm{rec}})$ and on the reconstruction parameters $(h_{\mathrm{ramp}}(u), m_\Lambda(\lambda, \gamma))$. Changing the speed of the time-attenuation curve and the rotation speed of the C-arm by the same factor $a > 1$, i.e.

$$\mu^{\mathrm{fast}}(\boldsymbol{x}, t) = \mu(\boldsymbol{x}, at) \tag{22}$$

$$\omega_{\mathrm{s}}^{\mathrm{fast}} = a\,\omega_{\mathrm{s}}\,, \tag{23}$$

does not change the artifact function $\chi_{\mathrm{art}}(\boldsymbol{s}, \boldsymbol{x}, t_{\mathrm{rec}})$. However, if only the C-arm rotation speed is increased while the time-attenuation curve remains constant then the artifact function changes. The change is non-linear and the weights of the higher-order DWPSFs is less than when compared to the weights of the lower-order DWPSFs. It can also be seen that

$$\lim_{\omega_{\mathrm{s}} \to \infty} \chi_{\mathrm{art}}(\boldsymbol{s}, \boldsymbol{x}, \lambda_{\mathrm{rec}}) = 0 \tag{24}$$

which means that the artifact disappears if the acquisition time interval becomes very short. Figure 3 shows the n-th order DWPSFs computed for typical scan and reconstruction parameters (Table 1). For better visualization, the windowing is set relative to their absolute amplitudes f_n defined as

$$f_n(\boldsymbol{x}, \lambda_{\mathrm{rec}}) = \max\left(\,|P_n(\boldsymbol{s}, \boldsymbol{x}, \lambda_{\mathrm{rec}})|\,\right)\,. \tag{25}$$

The 0-th order DWPSF describes the normal blurring of a point object due to the scan and reconstruction process. The integral value over the function P_0 is close to unity whereas the integral values over P_n with odd n are close to zero. Interestingly, the DWPSFs with odd values for n and even values for n have similar patterns, respectively.

The pattern can be explained by investigation of Equation (17). In this equation only the factor $l_n(\lambda) \equiv \lambda^n/n!$ depends on n. For $n = 0$ this factor is a constant and all view-angles contribute equally to the integral value. For $n > 0$ the function $l_n(\lambda)$ introduces a non-uniform view-angle-dependent weighting. If n is odd then $l_n(\lambda)$ is an odd function and the values at the integral endpoints have different signs. If n is even then the values of $l_n(\lambda)$ are equal at the integral endpoints. These properties cause similar functions $P_n(\boldsymbol{s}, \boldsymbol{x}, \lambda_{\mathrm{rec}})$ for even and odd n, respectively.

We will now investigate the variable λ_{rec}. If $\boldsymbol{x} = (0,0)^{\mathrm{T}}$ then $P_n(\boldsymbol{s}, \boldsymbol{x}, \lambda_{\mathrm{rec}})$ depends on λ_{rec} only by $\boldsymbol{s} \cdot \boldsymbol{e}_{\mathrm{u}}(\lambda + \lambda_{\mathrm{rec}})$ and $\boldsymbol{s} \cdot \boldsymbol{e}_{\mathrm{w}}(\lambda + \lambda_{\mathrm{rec}})$. We express $\boldsymbol{s}$ in polar coordinates as $\boldsymbol{s} = (r\cos(\phi),\, r\sin(\phi))^{\mathrm{T}}$ and using common trigonometric identities we get:

$$\boldsymbol{s} \cdot \boldsymbol{e}_{\mathrm{u}}(\lambda + \lambda_{\mathrm{rec}}) = r\,\sin(\phi - \lambda - \lambda_{\mathrm{rec}}) \tag{26}$$

$$\boldsymbol{s} \cdot \boldsymbol{e}_{\mathrm{w}}(\lambda + \lambda_{\mathrm{rec}}) = r\,\cos(\phi - \lambda - \lambda_{\mathrm{rec}})\,. \tag{27}$$

We can see that a change of the variable λ_{rec} by a certain angle can be compensated by a rotation of the coordinate system by the same angle in the opposite direction
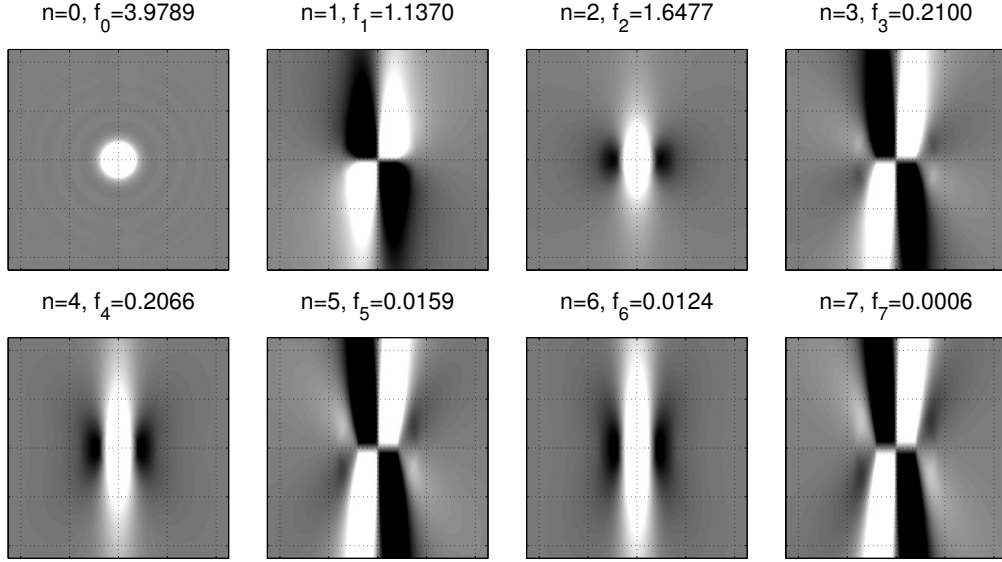
Figure 3. Plot of the derivative-weighted point spread functions $P_n(\boldsymbol{s}, (0,0)^{\mathrm{T}}, 0)$ computed from the parameters given in Table 1. The variable f_n is the absolute amplitude of P_n. The images have a windowing from $-f_n/2$ (black) to $+f_n/2$ (white) and their dotted grids have a spacing of 1 mm.

of rotation. Therefore, changing λ_{rec} results in a rotation of the function $P_n(\boldsymbol{s}, (0,0)^{\mathrm{T}}, \lambda_{\mathrm{rec}})$ around the origin. Generally, i.e. also for $\boldsymbol{x} \neq (0,0)^{\mathrm{T}}$, we can see that $P_n(\boldsymbol{s}, \boldsymbol{x}, \lambda_{\mathrm{rec}})$ is 2π periodic with respect to λ_{rec}.

4. Numerical example

In this section we will use our artifact model to predict artifacts from a typical temporal change of attenuation values in perfusion imaging. For validation we will compare the predictions from the model with numerical simulations. Finally, we will use the model for an analysis of different reconstruction parameter values.

4.1. Methods

We define a mathematical phantom $\mu_{\mathrm{pha}}(\boldsymbol{x}, t)$ to model a large cerebral artery inside the human head. It consists of two circles that are centered in the origin: a smaller circle with radius $r_{\mathrm{artery}} = 1$ mm and a larger circle with radius $r_{\mathrm{head}} = 100$ mm. In order to simulate contrast flow the attenuation values inside the smaller circle vary over time t according to a function $\mu_{\mathrm{artery}}(t)$ proposed by Østergaard et al. (1996):

$$\mu_{\mathrm{pha}}(\boldsymbol{x}, t) = \begin{cases} \mu_{\mathrm{water}} + \mu_{\mathrm{artery}}(t) & \text{if } x^2 + y^2 \leq r_{\mathrm{artery}}^2 \\ \mu_{\mathrm{water}} & \text{if } r_{\mathrm{artery}}^2 < x^2 + y^2 \leq r_{\mathrm{head}}^2 \\ 0 & \text{otherwise} \end{cases} \tag{28}$$

with

$$\mu_{\mathrm{artery}}(t) = \frac{A}{(\alpha\,\beta\,\exp(-1))^\alpha}\,\tau^\alpha\,\exp(-\tau/\beta)\,H(\tau)\,. \tag{29}$$
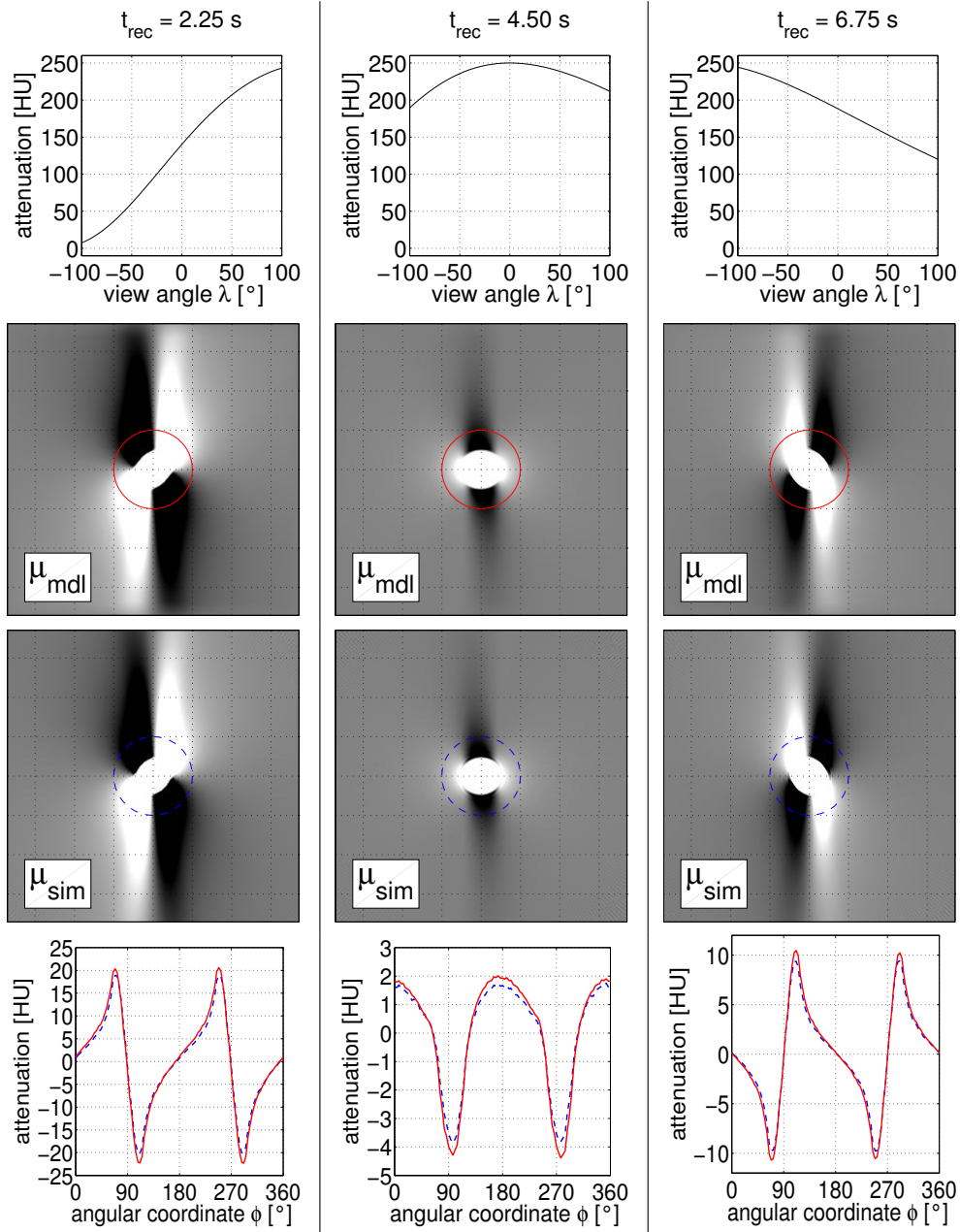
Figure 4. Examples for artifacts due to inconsistent data: (1st row) view-angle-dependent attenuation value inside the modeled origin-centered artery with radius 1 mm, (2nd row) predicted reconstruction using the artifact model, (3rd row) reconstruction using numerical simulations, (4th row) plot of attenuation values along the circular paths shown in the above images (μ_{mdl} ——, μ_{sim} - - - -). The images have a windowing from –5 HU (black) to +5 HU (white) and their dotted grids have a spacing of 2.5 mm.

Table 1. C-arm CT scan and reconstruction parameters used for the numerical examples.

parameter	symbol	value
starting view-angle	λ_0	$-100°$
view-angle increment	$\Delta\lambda$	$1°$
number of views per rotation	N_{views}	201
angular range per rotation	$\Lambda = (N_{\text{views}} - 1) \times \Delta\lambda$	$200°$
angular velocity of the C-arm	ω_{s}	$60\ °/\text{s}$
time per rotation	$T_{\text{rot}} = \Lambda/\omega_{\text{s}}$	3.33 s
source-to-isocenter distance	R	800 mm
source-to-detector distance	D	1200 mm
number of detector pixels	N_{detpix}	600
detector pixel size	Δu	0.6 mm
total detector width	$U = N_{\text{detpix}} \times \Delta u$	360 mm
full fan-angle	$\gamma_{\text{m}} = 2\arctan(U/(2\,D))$	$17.1°$
redundancy weighting function	m_Λ	see Equation (9)
ramp filter kernel	h_{ramp}	Shepp-Logan, see Kak & Slaney (1988)
number of reconstructed pixels		301×301
reconstructed pixel size		$0.015 \times 0.015\ \text{mm}^2$

$H(\tau)$ is the unit step function, $\mu_{\text{water}} = 0.18\,\text{cm}^{-1}$ is the X-ray attenuation of water, $A = 0.25\,\mu_{\text{water}}$ is the maximum enhancement, $\alpha = 3.0$ and $\beta = 1.5$ are shape parameters and $\tau = t/\text{s}$ is a dimensionless quantity where s denotes seconds.

We compute the image $\mu_{\text{mdl}}(\boldsymbol{x}, t_{\text{rec}})$ using the artifact model. According to Equation (11) the final 2-D reconstruction μ_{rec} is a superposition of the 2-D functions χ which can be thought of as individual reconstructions of (theoretical) point objects. To apply our artifact model, we first approximate the point objects by discrete pixels. Then we compute χ for each pixel and determine μ_{rec} using a discretized version of Equation (11).

In order to compute χ we consider only the first four functions P_n $(n = 0, \ldots, 3)$ assuming 4-th and higher order derivative values can be neglected due to the smoothness of $\mu_{\text{artery}}(t)$. The parameters for the model are taken from Table 1. The reconstruction time points t_{rec} are 2.25 s, 4.50 s and 6.75 s. We choose these time points to investigate the reconstruction from data acquired during the inflow, plateau and outflow phase of the time curve (see first row in Figure 4). We assume that the data was acquired from three individual C-arm rotations which all started at the same starting angle to allow for better comparison.

For the numerical simulation we use the scan parameters from Table 1 to simulate C-arm CT scanning of the central slice of the phantom during the time interval $t \in [t_{\text{rec}} - T_{\text{rot}}/2,\ t_{\text{rec}} + T_{\text{rot}}/2]$. The reconstruction time points t_{rec} are the same as for the artifact model. A FBP reconstruction $\mu_{\text{sim}}(\boldsymbol{x}, t_{\text{rec}})$ is generated from the simulated projections by applying the reconstruction parameters from Table 1.

4.2. Results and Discussion

In Figure 4 each column corresponds to a different time t_{rec}. The first row shows a plot of the view-angle-dependent attenuation value inside the artery. The second and third rows show the images μ_{mdl} and μ_{sim} respectively. The last row shows values of μ_{mdl} and μ_{sim} evaluated along a circular path (radius 2.5 mm) around the origin of the
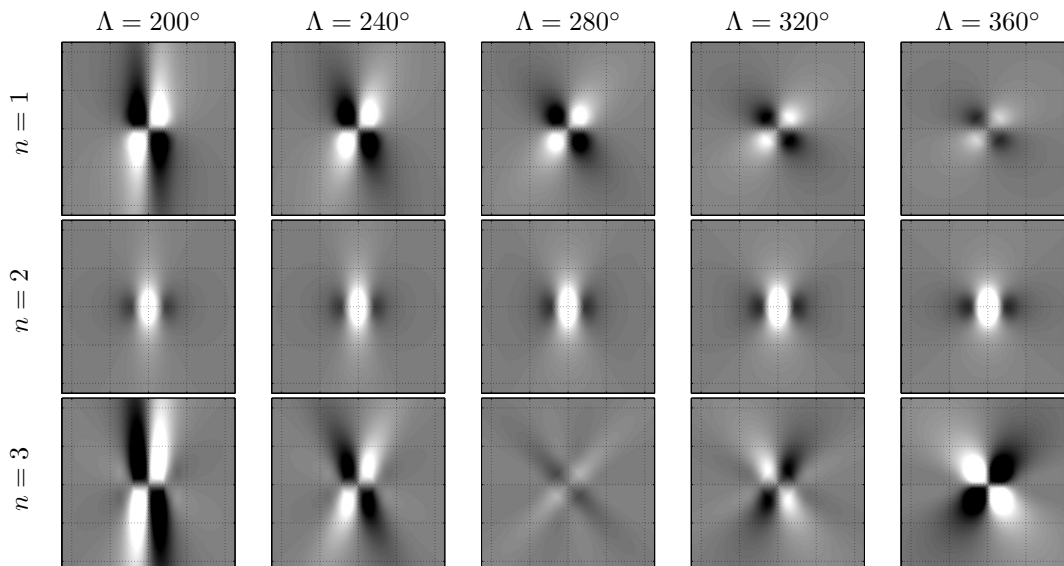
Figure 5. Derivative-weighted point spread functions P_n of the artifact model computed for different sliding window length Λ. The window center is 0 and the window widths are constant for each n (see text for details). The colormap range is from black to white. The dotted grid has a spacing of 1 mm.

coordinate system. This path is also depicted in the images in the second and third row. The windowing of the images was chosen from –5 HU to +5 HU. Because the contrast enhancement in tissue is about 5 to 10 HU — given an arterial enhancement of 250 HU and a blood volume fraction in cerebral tissue of 2% to 4% — this windowing is useful to estimate the areas where the artifact values have the same magnitude as the peaks of the tissue time-attenuation curves.

The results from the model (μ_{mdl}) and the simulation (μ_{sim}) show excellent agreement. The curves in the last row of Figure 4 have root mean square deviations of 1.1 HU ($t_{\mathrm{rec}} = 2.25$ s), 0.3 HU ($t_{\mathrm{rec}} = 4.50$ s) and 0.5 HU ($t_{\mathrm{rec}} = 6.75$ s). The model has also been validated with other reconstruction parameters and temporal dynamics and we obtained similar results (data not shown). From the results we can see that only a small number of DWPSFs of the model must be considered in order to predict the artifacts from typical perfusion time-attenuation curves. The small differences between model and simulation are primarily due to discretization effects.

4.3. Analysis of reconstruction parameters

Our model can be used to systematically analyze the effect of different scan and reconstruction parameters on the artifacts from inconsistent data. Parameters that could be investigated include, for example, the filter kernel $h_{\mathrm{ramp}}(u)$, the type of the redundancy weighting function $m_\Lambda(\lambda, \gamma)$ and the sliding window length Λ.

As an example, we present the DWPSFs computed for different sliding window lengths Λ. We use the parameters from Table 1, change the value for N_{views} and adapt Λ accordingly. The windowing function $w_\Lambda(\lambda, 0)$ for different Λ is shown in Figure 6(a) and Figure 5 shows P_n ($n = 1, 2, 3$) computed for different Λ. The window

(a) Sliding window function $w_\Lambda(\lambda, 0)$.

(b) Weighted spatial spread S_n of P_n.
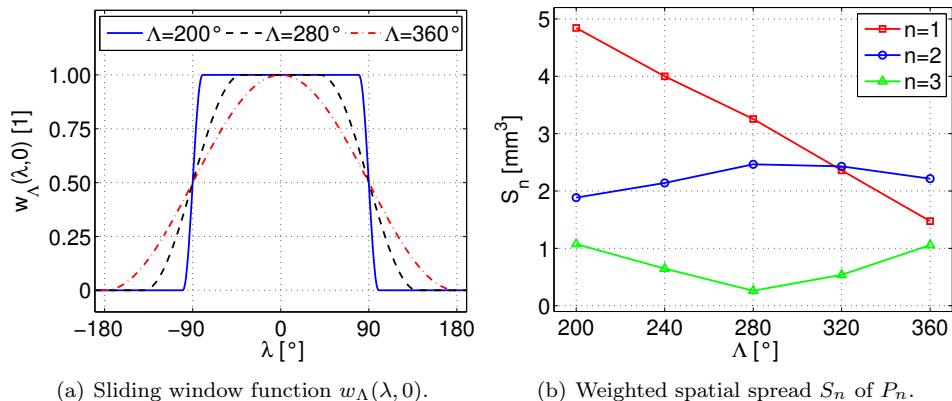
Figure 6. (a) Sliding windowing function $w_\Lambda(\lambda, 0)$ corresponding to the central ray for different Λ. (b) Weighted spatial spread S_n of P_n depending on Λ.

width is constant for each n for better comparison of the change due to different Λ. We set the window widths to the maximum absolute amplitude values f_n, computed for $\Lambda = 200°$ as shown in Figure 3.

For quantitative evaluation we introduce the weighted spatial spread S_n of P_n which we define as

$$S_n(\boldsymbol{x}, \lambda_{\mathrm{rec}}) = \iint |P_n(\boldsymbol{s}, \boldsymbol{x}, \lambda_{\mathrm{rec}})| \, (s_x^2 + s_y^2)^{1/2} \, \mathrm{d}s_x \, \mathrm{d}s_y \, . \tag{30}$$

This heuristic definition takes into account both the absolute HU value of the artifact and its distance from the center of the point object and can be used for relative comparison of different Λ values. We are computing the absolute value of P_n in order to avoid the possibility that positive and negative contributions of P_n cancel each other out. Because artifacts which propagate farther into the tissue area can have a more negative impact on the clinical interpretation of the perfusion maps we have also included a distance weighting.

Figure 6(b) shows that increasing the sliding window length reduces S_1 from 4.84 mm^3 ($\Lambda = 200°$) to 1.48 mm^3 ($\Lambda = 360°$). Interestingly, S_3 increases from 0.26 mm^3 ($\Lambda = 280°$) to 1.06 mm^3 ($\Lambda = 360°$). The behavior of the functions P_n with respect to Λ and other reconstruction parameters can be explained by investigation of Equation (17) which, however, will not be covered by this paper.

We can use the artifact model to optimize reconstruction parameters for the expected temporal variation of the attenuation values. The spatial spread of the linear component a of the time-attenuation curve, defined by S_1, decreases by about 70% when using $\Lambda = 360°$ compared to $\Lambda = 200°$. Typically, one can find an approximately linear change of attenuation inside an arterial vessel during the inflow phase.

Therefore, with respect to the spatial spread of the FBP artifacts the parameter value $\Lambda = 360°$ is more optimal than $\Lambda = 200°$ if the dynamic changes of the attenuation values are approximately piecewise linear. On the other hand, for temporal dynamics that are not expected to be piecewise linear, different Λ values may be more optimal. Note that, a larger window length would not increase the total X-ray dose during the exam if continuously rotating C-arm CT systems could be used.

(a) reference   (b) forward rotation   (c) backward rotation
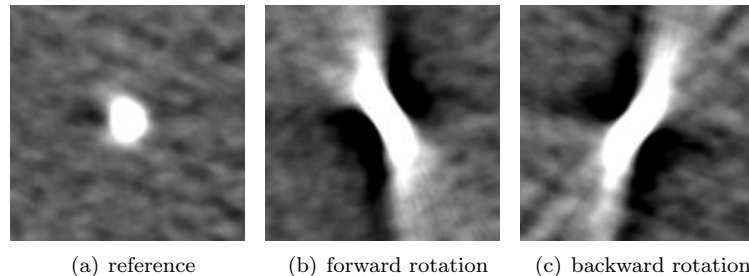
Figure 7. Reconstructions of a flow phantom: (a) reference reconstruction of data with constant attenuation values and (b-c) reconstructions of data acquired during a forward and backward C-arm rotation while the attenuation values inside the plastic tube were linearly increasing. The windowing is from -250 HU (black) to +250 HU (white).

Higher Λ values lead to a lower temporal resolution of the reconstructed time-attenuation curves. Although the full width at half maximum is the same for all windows $w_\Lambda(\lambda, 0)$, see Figure 6(a), the full width at quarter maximum, for example, increases for higher Λ. We note that there is a trade-off between the reduction of the spatial spread of the artifacts and the temporal resolution of the reconstructed time curves; this topic will be subject of future investigation.

5. Experimental Data From a Clinical C-arm CT

In this section, we present reconstruction results of a flow phantom with time-varying attenuation values that was scanned using a clinical C-arm CT system.

5.1. Methods

In order to investigate reconstruction artifacts due to time-varying attenuation values under realistic conditions we have built a simple flow phantom. We have placed a small plastic tube (inner diameter 2.0 mm) into a water-filled container (volume of water about $22 \times 8 \times 25$ cm^3) that was placed on the patient table of a clinical C-arm CT system (Artis dTA with DynaCT, Siemens AG, Healthcare Sector, Forchheim, Germany). The tube was connected to a double head contrast injector (Accutron HP-D, Medtron AG, Saarbrücken, Germany) that had the syringes filled with water and contrast agent (Oxilan 300, Guerbet Group, Villepinte, France), respectively. During injection into the tube (injection rate 10 ml/s) the mixing ratio of the two syringes was linearly changed from 0% to 50% contrast agent using an increase of 12.5% contrast agent per second.

We acquired 191 projections with a view-angle increment of $1.0°$, a detector pixel spacing of 0.616×0.616 mm^2 after 4×4 binning and a C-arm rotation time of 4.3 seconds. The phantom was scanned using a forward and a backward C-arm rotation and one 3-D volume was reconstructed for each rotation with the standard reconstruction filter kernel. For reference, the phantom filled with a constant amount (about 15%) of contrast agent was also scanned and reconstructed.

5.2. Results and Discussion

Figure 7 shows the reference reconstruction of the static phantom data and the two reconstructions of the dynamic phantom data from the forward and backward C-arm rotation, respectively. The axial images were reconstructed using 150×150 pixels with 0.1 mm pixel spacing. Thus, the side length of each image is 15 mm. The reconstructions show a similar pattern when compared with the reconstruction of the numerical phantom during the inflow or outflow phase (Figure 4, left and right columns) which also resulted from an approximately linear change of attenuation values during the data acquisition.

Using our artifact model, we can interpret the reconstruction results in Figure 7(b)-(c) as the superposition of the weighted DWPSFs of zeroth (P_0) and first (P_1) order. We assume that second and higher order DWPSFs receive zero weights due to the approximately linear change of attenuation values. The different signs of the streaks in Figure 7(b)-(c), which are contributions of P_1, are well explained by the different directions of the C-arm rotation, i.e. different signs of ω_s. Note that, the weight of P_0 is independent of ω_s, see Equation (15).

This experiment provides a qualitative evaluation and interpretation of the reconstruction artifacts of the flow phantom. A more detailed, quantitative analysis could be carried out in the future. For example, different angular sliding window lengths up to $360°$ could be investigated. With potential future C-arm CT systems that could perform continuous C-arm rotations this investigation would be of high interest in order to validate the predictions from the numerical example in Section 4.3.

6. Discussion and summary

The aim of this work was to derive and interpret a model for FBP reconstruction artifacts due to time-varying attenuation values. We analyzed the FBP algorithm because it is computationally very fast and can be applied to reconstruct large-volume data sets in C-arm CT perfusion imaging during stroke treatment.

Our novel spatio-temporal model describes the variation of attenuation values by their temporal derivative values. To model the spatial spread of the artifacts we introduced time-derivative-weighted point spread functions which are computed from the scan and reconstruction parameters. With this formalism the reconstruction artifacts can be separated into a component that depends on the dynamic process and a component that purely depends on system parameters. The model is optimized for contrast flow in perfusion imaging where the dynamic process can be approximated by a few temporal derivative values.

Our model gives a detailed understanding of these FBP reconstruction artifacts. It can be used to predict the magnitude of artifacts for different temporal dynamics if the scan and reconstruction parameters are known. The model can also be applied to further investigate different reconstruction parameters in a systematic way. As a first example, we have shown a comparison of different reconstruction sliding window lengths Λ. It could be seen that the optimal value for Λ depends on the expected temporal dynamics of the attenuation values.

A limitation of our model is that artifacts due to sudden changes of the local attenuation values, caused for example by patient motion cannot be well described. These artifacts, which are most prominent at regions that have a high spatial gradient of attenuation values, can degrade the image quality in a similar manner as the artifacts

due to contrast flow. In order to model these artifacts a higher number of DWPSFs would be required, to consider more terms of the Taylor series, which would however not be practical. Alternatively, if our artifact model was adapted such that it would use a parameterization of the time-attenuation curves which allows sudden changes of the attenuation values it may be possible to adequately describe these artifacts as well.

Noise in projection images was not considered in the artifact model. It can be treated by separating the noise from the signal and then making a normal FBP reconstruction of the noise. The artifact model is applied to the signal only. The final result of the model is the sum of the prediction from the noise-free signal and the reconstruction of the noise.

In this paper, the model has been derived for the direct 2-D fan-beam FBP. To derive it for reconstruction algorithms that use 3-D cone-beam data, like the FDK algorithm (Feldkamp et al. 1984), the equations in Section 2 must be extended to the 3-D geometry and the equations in Section 3 must be derived in a similar approach using this new geometry.

All terms in the artifact model are linear and this model could be written as a matrix equation if Equations (11), (15) and (17) were discretized and the derivatives were approximated by discrete derivative operators. Hence, a numerical inversion of this model could used to reduce the artifacts in the reconstructed images. Considering only those terms corresponding to $n = 1$ and $n = 2$ would make the inversion approach robust against noise while still including the most relevant terms.

To summarize, our novel model provides a comprehensive method to describe FBP artifacts from time-varying attenuation values in perfusion imaging. It is a mathematically exact analysis of the FBP reconstruction algorithm. This model can lead to enhanced reconstruction approaches in interventional perfusion imaging, such as sliding-window reconstruction approaches for continuously-rotating C-arm CT systems, in order to optimize patient treatment during stroke therapy procedures.

Acknowledgments

Appendix A.

To derive Equation (11) and Equation (12) we first evaluate the delta function in Equation (10) using the identity

$$\int f(u)\,\delta(u^*(\boldsymbol{x}, \lambda(t)) - u)\,\mathrm{d}u = f(u^*(\boldsymbol{x}, \lambda(t))) \tag{A.1}$$

and then split the result into the following two functions:

$$\mu_{\mathrm{rec}}(\boldsymbol{r}, t_{\mathrm{rec}}) = \iint \hat{\chi}(\boldsymbol{r}, \boldsymbol{x}, t_{\mathrm{rec}})\,\mathrm{d}x\,\mathrm{d}y \tag{A.2}$$

$$\hat{\chi}(\boldsymbol{r}, \boldsymbol{x}, t_{\mathrm{rec}}) = \int \frac{R\,D^2}{(R - \boldsymbol{r} \cdot \boldsymbol{e}_{\mathrm{w}}(\lambda(t)))^2}\, h_{\mathrm{ramp}}\Big(u^*(\boldsymbol{r}, \lambda(t)) - u^*(\boldsymbol{x}, \lambda(t))\Big)$$
$$\times\, \mu\Big(\boldsymbol{x}, \lambda(t)\Big) \left((u^*(\boldsymbol{x}, \lambda(t)))^2 + D^2\right)^{-1/2}$$

$$\times w_\Lambda\left(\lambda(t) - \lambda(t_{\rm rec}), \arctan(u^*(\boldsymbol{x}, \lambda(t))/D)\right) {\rm d}t \, . \tag{A.3}$$

By re-writing $\hat{\chi}(\boldsymbol{r}, \boldsymbol{x}, t_{\rm rec})$ such that it depends on the distance vector $\boldsymbol{s} = \boldsymbol{r} - \boldsymbol{x}$ we get the expressions shown in Equation (11) and Equation (12).

Appendix B.

We want to prove that the n-th order total derivative of a function $\mu(\lambda(t))$, which has the property ${\rm d}^2\lambda/{\rm d}t^2 = 0$, is given by

$$\frac{{\rm d}^n\mu}{{\rm d}t^n} = \frac{\partial^n\mu}{\partial\lambda^n}\left(\frac{{\rm d}\lambda}{{\rm d}t}\right)^n \, . \tag{B.1}$$

First we define

$$D_k \equiv \frac{\partial^k\mu}{\partial\lambda^k}\left(\frac{{\rm d}\lambda}{{\rm d}t}\right)^k \, . \tag{B.2}$$

By applying the product rule of differentiation we get

$$\frac{{\rm d}}{{\rm d}t}D_k = \frac{{\rm d}}{{\rm d}t}\frac{\partial^k\mu}{\partial\lambda^k}\left(\frac{{\rm d}\lambda}{{\rm d}t}\right)^k + \frac{\partial^k\mu}{\partial\lambda^k}\frac{{\rm d}}{{\rm d}t}\left(\frac{{\rm d}\lambda}{{\rm d}t}\right)^k \, . \tag{B.3}$$

We can re-arrange the first term in Equation (B.3) to

$$\begin{aligned}
\frac{{\rm d}}{{\rm d}t}\frac{\partial^k\mu}{\partial\lambda^k}\left(\frac{{\rm d}\lambda}{{\rm d}t}\right)^k &= \frac{\partial^k}{\partial\lambda^k}\frac{{\rm d}\mu}{{\rm d}t}\left(\frac{{\rm d}\lambda}{{\rm d}t}\right)^k \\
&= \frac{\partial^k}{\partial\lambda^k}\left(\frac{\partial\mu}{\partial\lambda}\frac{{\rm d}\lambda}{{\rm d}t}\right)\left(\frac{{\rm d}\lambda}{{\rm d}t}\right)^k \\
&= \frac{\partial^{k+1}\mu}{\partial\lambda^{k+1}}\left(\frac{{\rm d}\lambda}{{\rm d}t}\right)^{k+1} \\
&= D_{k+1} \, . \tag{B.4}
\end{aligned}$$

Re-writing the second term in Equation (B.3) gives

$$\frac{\partial^k\mu}{\partial\lambda^k}\frac{{\rm d}}{{\rm d}t}\left(\frac{{\rm d}\lambda}{{\rm d}t}\right)^k = \frac{\partial^k\mu}{\partial\lambda^k}\left(k\left(\frac{{\rm d}\lambda}{{\rm d}t}\right)^{k-1}\frac{{\rm d}^2\lambda}{{\rm d}t^2}\right) = 0 \, . \tag{B.5}$$

In the last equation we used that the second order derivative of $\lambda(t)$ is zero. Combining Equation (B.3), Equation (B.4) and Equation (B.5) yields

$$\frac{{\rm d}}{{\rm d}t}D_k = D_{k+1} \, . \tag{B.6}$$

The n-th order derivative of D_k can be expressed by applying Equation (B.6) iteratively:

$$\frac{{\rm d}^n}{{\rm d}t^n}D_k = D_{k+n} \, . \tag{B.7}$$

Now, we can show that for $n \geq 1$ we get

$$\frac{{\rm d}^n\mu}{{\rm d}t^n} = \frac{{\rm d}^{n-1}}{{\rm d}t^{n-1}}\frac{{\rm d}\mu}{{\rm d}t} = \frac{{\rm d}^{n-1}}{{\rm d}t^{n-1}}D_1 = D_{1+(n-1)} = \frac{\partial^n\mu}{\partial\lambda^n}\left(\frac{{\rm d}\lambda}{{\rm d}t}\right)^n \, , \tag{B.8}$$

which is the same expression as in Equation (B.1).

References

Bok B D, Bice A N, Clausen M, Wong D F & Wagner H N 1987 'Artifacts in camera based single photon emission tomography due to time activity variation' *European Journal of Nuclear Medicine* **13**(9), 439–442.

Fahrig R 1999 Computed Rotational Angiography: Use of a C-arm-Mounted XRII for 3D Imaging of Intracranial Vessels during Neuro-interventional Procedures PhD thesis University of Western Ontario, London, ON, Canada.

Feldkamp L A, Davis L C & Kress J W 1984 'Practical cone-beam algorithm' *Journal of the Optical Society of America* **A1**, 612–619.

Fieselmann A, Ganguly A, Deuerling-Zheng Y, Zellerhoff M, Boese J, Hornegger J & Fahrig R 2010 'A dynamic reconstruction approach for cerebral blood flow quantification with an interventional C-arm CT' *in* 'Proc. IEEE Int Symp Biomed Imaging 2010' Rotterdam, The Netherlands pp. 53–56.

Garden K L, Bates R, Won M & Chikwanda H 1984 'Computerized tomographic imaging is insensitive to density variation during scanning' *Image and Vision Computing* **2**(2), 76–84.

Holden J E & Ip W R 1978 'Continuous time-dependence in computed tomography' *Medical Physics* **5**(6), 485–490.

Ip W R, Holden J E & Winkler S S 1983 'A study of image discrepancies due to object time-dependence in transmission and emission tomography' *Physics in Medicine and Biology* **28**(8), 953–962.

Kak A C & Slaney M 1988 *Principles of Computerized Tomographic Imaging* IEEE Press New York.

Montes P & Lauritsch G 2007 'A temporal interpolation approach for dynamic reconstruction in perfusion CT' *Medical Physics* **34**(7), 3077–3092.

Nakajima K, Shuke N, Taki J, Ichihara T, Motomura N, Bunko H & Hisada K 1992 'A simulation of dynamic SPECT using radiopharmaceuticals with rapid clearance' *Journal of Nuclear Medicine* **33**(6), 1200–1206.

Neukirchen C, Giordano M & Wiesner S 2010 'An iterative method for tomographic x-ray perfusion estimation in a decomposition model-based approach' *Medical Physics* **37**(12), 6125–6141.

Ohkubo M, Wada S, Ida S, Kunii M, Kayugawa A, Matsumoto T, Nishizawa K & Murao K 2009 'Determination of point spread function in computed tomography accompanied with verification' *Medical Physics* **36**(6), 2089–2097.

Rohkohl C, Keck B, Hofmann H & Hornegger J 2009 'RabbitCT – an open platform for benchmarking 3D cone-beam reconstruction algorithms' *Medical Physics* **36**(9), 3940–3944.

Shetty S K & Lev M H 2006. *Acute Ischemic Stroke: Imaging and Intervention* 1st edn Springer Berlin, Germany chapter CT Perfusion (CTP), pp. 87–113.

Silver M D 2000 'A method for including redundant data in computed tomography' *Medical Physics* **27**(4), 773–774.

Østergaard L, Weisskoff R M, Chesler D A, Gyldensted C & Rosen B R 1996 'High resolution measurement of cerebral blood flow using intravascular tracer bolus passages. part I: Mathematical approach and statistical analysis' *Magnetic Resonance in Medicine* **36**(5), 715–725.

Strobel N, Meissner O, Boese J, Brunner T, Heigl B, Hoheisel M, Lauritsch G, Nagel M, Pfister M, Rührnschopf E P, Scholz B, Schreiber B, Spahn M, Zellerhoff M & Klingenbeck-Regn K 2009. *Multislice CT* 3rd edn Springer Berlin, Germany chapter 3D Imaging with Flat-Detector C-Arm Systems, pp. 33–51.

Wintermark M, Smith W S, Ko N U, Quist M, Schnyder P & Dillon W P 2004 'Dynamic perfusion CT: optimizing the temporal resolution and contrast volume for calculation of perfusion CT parameters in stroke patients.' *American Journal of Neuroradiology* **25**(5), 720–729.

Zeng G L 2004 'Nonuniform noise propagation by using the ramp filter in fan-beam computed tomography' *IEEE Transactions on Medical Imaging* **23**(6), 690–695.